ACS OMEGA

Article

http://pubs.acs.org/journal/acsodf

Origin of High-Efficiency Photoelectrochemical Water Splitting on Hematite/Functional Nanohybrid Metal Oxide Overlayer Photoanode after a Low Temperature Inert Gas Annealing Treatment

SocMan Ho-Kimura,*,†,# Benjamin A. D. Williamson,†,‡ Sanjayan Sathasivam,† Savio J. A. Moniz,§ Guanjie He,† Wenjun Luo,§,⊥ David O. Scanlon,†,‡,∥ Junwang Tang,§ and Ivan P. Parkin*,†

†Department of Chemistry, University College London, 20 Gordon Street, London WC1H 0AJ, U.K.

‡Thomas Young Centre, University College London, Gower Street, London WC1E 6BT, U.K.

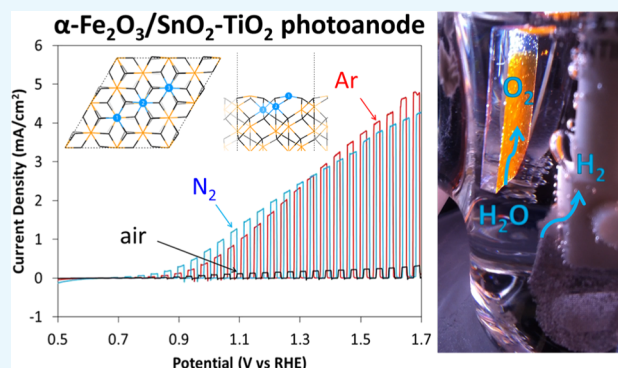§Department of Chemical Engineering, University College London, Torrington Place, London WC1E 7JE, U.K.

∥Diamond Light Source Ltd., Diamond House, Harwell Science and Innovation Campus, Didcot, Oxfordshire OX11 0DE, U.K.

⊥Ecomaterials and Renewable Energy Research Center (ERERC), National Laboratory of Solid State Microstructures, and College of Engineering and Applied Sciences, Nanjing University, Nanjing 210093, P. R. China

#Institute of Applied Physics and Materials Engineering, University of Macau, Avenida da Universidade, Taipa, Macau SAR, China

S *Supporting Information*

ABSTRACT: A simplistic and low-cost method that dramatically improves the performance of solution-grown hematite photoanodes for solar-driven water splitting through incorporation of nanohybrid metal oxide overlayers was developed. By heating the α-Fe$_2$O$_3$/SnO$_2$−TiO$_2$ electrode in an inert atmosphere, such as argon or nitrogen, the photocurrent increased to over 2 mA/cm^2 at 1.23 V versus a reversible hydrogen electrode, which is 10 times higher than that of pure hematite under 1 sun (100 mW/cm^2, AM 1.5G) light illumination. For the first time, we found a significant morphological difference between argon and nitrogen gas heat-treated hematite films and discussed the consequences for photoresponse. The origin for the enhancement, probed via theoretical modeling, stems from the facile incorporation of low formation energy dopants into the Fe$_2$O$_3$ layer at the interface of the metal oxide nanohybrid overlayer, which decreases recombination by increasing the electrical conductivity of Fe$_2$O$_3$. These dopants diffuse from the overlayer into the α-Fe$_2$O$_3$ layer readily under inert gas heat treatment. This simple yet effective strategy could be applied to other dopants to increase hematite performance for solar energy conversion applications.

INTRODUCTION

Hematite (α-Fe$_2$O$_3$) thin films have been actively investigated for photoelectrochemical (PEC) water splitting because of their narrow band gap of approximately 1.9−2.2 eV, their sufficiently deep valence band position for water oxidation, and high relative existence of hematite in the earth's crust. It has been reported to possess a maximum theoretical photocurrent of 12.6 mA/cm^2 at 1.23 V versus a reversible hydrogen electrode (RHE) under 1 sun illumination and a theoretical solar-to-hydrogen (STH) efficiency of 12.9−15.3%.[1−3] However, hematite suffers from poor charge transport capacity with a short hole diffusion length of 2−4 nm, thus making recombination a severe limiting factor.[4−6] To improve the STH conversion efficiency, charge separation and surface reaction kinetics need to be enhanced. This can be achieved in

several ways, for example, through morphology variation,[7] the addition of dopants,[7−13] and cocatalysts on the surface.[5,6] The latter two techniques introduce passivating surface states which can decrease surface recombination at low photovoltages. In terms of bulk dopants, which act to increase the electrical conducting properties of the photoanode, a number of metals/metal oxides have been combined with hematite, such as Pt[11] Ti[12] or SiO$_2$,[2,8] SnO$_2$,[7] and TiO$_2$.[13] Generally the addition of such dopants requires high temperatures (>600 °C) under oxidizing conditions, which can also cause the diffusion of SnO$_2$ from the fluorine-doped tin oxide (FTO) layer of the
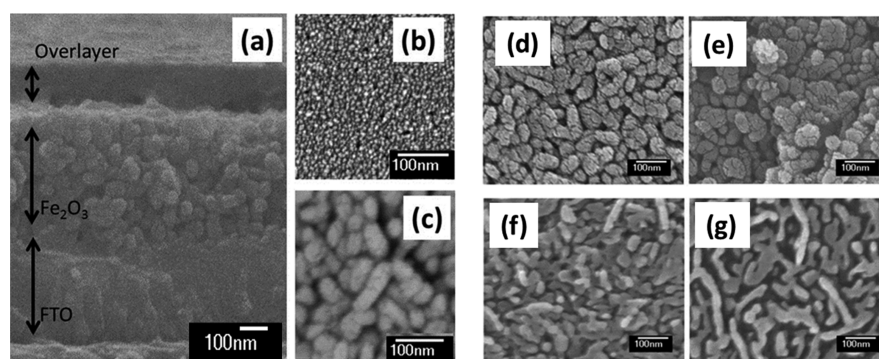
Figure 1. SEM images of FTO/α-Fe$_2$O$_3$/SnO$_2$–TiO$_2$ photoanode: (a) cross-section, (b) surface of the SnO$_2$–TiO$_2$ overlayer, and (c) bare α-Fe$_2$O$_3$ before inert gas treatment and after inert gas annealing treatment for 1 h in (d) N$_2$ at 500 °C, (e) N$_2$ at 550 °C, (f) Ar at 500 °C, and (g) Ar at 550 °C.
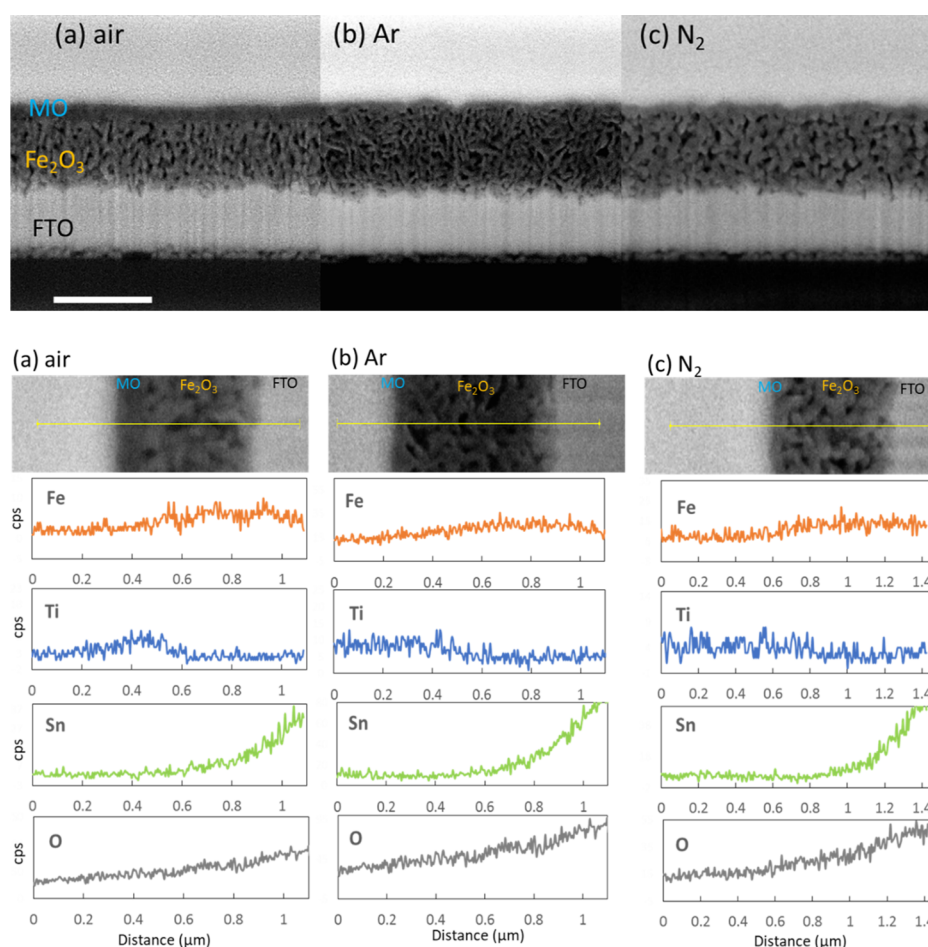

Figure 2. FIB-SEM images and EDS elemental distribution of α-Fe$_2$O$_3$/SnO$_2$–TiO$_2$ films (a) before and after 1 h treatment in (b) Ar gas and (c) N$_2$ gas at 500 °C. MO: metal oxide overlayer. The scale bar is 500 nm.

substrate into the hematite film with a consequential increase in donor density and conductivity.[7,14,15] In cases where Sn is used as a dopant from the FTO substrate in high temperature (>600 °C) treatment methods, there is limited control over dopant concentration in the hematite layer, thus resulting in poor device performance. As such, there is a need for a simpler, more cost-effective method of modifying hematite photoanodes for enhanced activity, and more work is needed to understand the role of dopants and overlayers. There are many reported synthetic routes for hematite synthesis at low temperature (<700 °C), such as magnetron sputtering,[6]

atmospheric pressure chemical vapor deposition,[16] and atomic layer deposition (ALD).[17] Electrodeposition is a popular solution-based technique; however, there are comparably fewer reports of hematite synthesis by electrodeposition, which is surprising given its comparative low-cost and scalability. Herein, we report an easy, affordable method to prepare robust α-Fe$_2$O$_3$/SnO$_2$–TiO$_2$ layered photoanodes, which exhibit significantly higher photocurrents than pure α-Fe$_2$O$_3$. Surprisingly, following a low temperature (≤500 °C) heat treatment of the α-Fe$_2$O$_3$/SnO$_2$–TiO$_2$ photoanodes in inert gas (argon or nitrogen), a near 10-fold increase in the

photocurrent compared to those heated in air was achieved. From scanning electron microscopy (SEM) images, there was an obvious morphological difference in the hematite after argon treatment and nitrogen treatment. The microstructure thermodynamics of the substitutional doping was elucidated using density functional theory (DFT) studies to investigate the reason for the enhanced activity. This revealed low formation energies at the surface compared to the bulk under experimental conditions indicating large dopant concentrations (Sn_{Fe} and Ti_{Fe}) at the interfaces that increase the conductivity. These results shed light on a new strategy to significantly enhance the activity of hematite photoanodes for efficient solar energy conversion to fuels. This uncomplicated inert gas heat treatment method can be applied to other hematite/dopant anodes.

■ RESULTS AND DISCUSSION

α-Fe_2O_3 (hematite) photoanodes were prepared by heating electrodeposited FeOOH (iron oxyhydroxide) films at 500 °C for 1 h. The SnO_2–TiO_2 metal oxide overlayer precursor solution was introduced by spin coating directly onto the α-Fe_2O_3 films. In SEM images (Figure 1a–c), the thickness of the α-Fe_2O_3 layer was ca. 300 nm, while the overlayer was ca. 100 nm. The host material α-Fe_2O_3 average particle size was ca. 25 nm in diameter. In the overlayer, very small SnO_2 and TiO_2 particles, ca. 5 nm in diameter, were also identified. This is because the precursor solution, peroxotitanic acid, is a thixotropic fluid which can also work as a medium, so that Sn precursors can mix into the Ti precursors easily, a phenomenon we observed previously during deposition of $BiVO_4$/TiO_2 films.[18] In this study, it is considered that the dopant particles are monodispersed and ultrafine, which is advantageous for the doping process. X-ray photoelectron spectroscopy (XPS) was used to elucidate the exact nature of the chemical species present in the α-Fe_2O_3/SnO_2–TiO_2 films, see Figure S1 (Supporting Information). From the Fe(III) 2p region, we observed Fe $2p_{3/2}$ at 710.8 eV, indicating the presence of Fe in the 3+ oxidation state.[19,20] For the samples containing overlayers, the metal oxide species were characterized for both Sn and Ti incorporation; with the Sn, the $3d_{5/2}$ peak was centered at 486.7 eV, matching the expected 4+ oxidation state,[21] and the Ti $2p_{3/2}$ transition was centered at 458.8 eV, corresponding to Ti^{4+}.[19,20]

In general, there is no significant effect on the morphology, crystallinity, and optical absorption of hematite even if it is heated at temperature ≤500 °C in air.[22] We first probed the effect of inert gas treatment on the morphology of the films. The SEM images (Figure 1d–g) reveal that before annealing in inert gas, the original α-Fe_2O_3 film exhibited a very porous morphology. After heat treatment in nitrogen, the particles appear to enlarge and coalesce; as such the particle size increase was proportional to the temperature. Following the heat treatment in argon, the morphology changed significantly. The particles fused together much more, resulting in a mesoporous-like structure. This was similar to the shape after 800 °C in air, which is reported in refs[2,7] From our XPS analysis at several positions of the bare α-Fe_2O_3 photoanodes, only following the heat treatment in argon did the Sn 3d peak of FTO glass disappear (Figure 2S), which suggests that the heat treatment in argon leads to significantly better coverage of the mesoporous hematite film. Furthermore, it was noted that no nitrogen species were detected by XPS analysis, indicating no chemical reaction with nitrogen. Focused ion beam-SEM

(FIB-SEM) with energy dispersive X-ray spectroscopy (EDS) cross-section analysis was conducted to explore the elemental distribution in the α-Fe_2O_3/SnO_2–TiO_2 films before and after inert gas treatment. Figure 2 (also see Figure 3S) displays the SEM images of the cross-section with EDS elemental distribution for the Fe, Ti, Sn, and O elements. With regard to the Fe_2O_3 particles, these agreed with that shown in Figure 1. Surprisingly, the nanohybrid metal oxide overlayer became thinner and almost disappeared after the treatment. In particular, it was clearly detected that the distribution peak of Ti spread uniformly in the treated porous hematite layer. In other words, it seems that the overlayer became an ultrafine protective shell on the surface of each hematite particle. Figure 3S indicates in detail the diminution of the Ti peak in the EDS spectra of the samples after the inert gas treatment. Metal oxides (SnO_2 and TiO_2) of the overlayer will not disappear by heating at a low temperature of 500 °C under inert gas. For this reason, Ti density was lowered to the detection limit level of the EDS after the inert gas treatment. It can be inferred that an extremely small amount of dopant is required for highly photoactive Fe_2O_3 anode.

The lattice parameters of bare α-Fe_2O_3, α-Fe_2O_3/TiO_2, and α-Fe_2O_3/SnO_2 films were calculated from X-ray diffraction (XRD) patterns (Figure 4S–6S and Table 1S). We found that the lattice volume decreased after inert gas treatment. For example, in the case of bare Fe_2O_3, the lattice volume was 303.11 Å in air, and after Ar and N_2 treatment, it became 302.70 and 302.71 Å, respectively. Likewise, the lattice volume of Fe_2O_3/SnO_2 changed from 302.78 Å (air) to 302.41 Å (Ar) and 302.59 Å (N_2); the lattice volume of Fe_2O_3/TiO_2 changed from 302.75 Å (air) to 302.44 Å (Ar) and 302.60 Å (N_2). Previous reports have described that the unit cell length of pure α-Fe_2O_3 enlarges as a function of the annealing temperature in air.[23] After inert gas treatment, the volume decreased due to site distortion of the bare α-Fe_2O_3. In general, the smaller the crystal size, the lower is the average site distortion.[23] Consequently, when Ti or Sn was doped into the Fe_2O_3 unit cell, it is thought that crystal lattice distortion was mitigated by the dopants. According to previous reports, when the crystal distortion change after doping is small, the appearance of the material does not change but the conductivity improves.[7,9] In Figure 7S, there is no big change in the XRD pattern of Fe_2O_3/SnO_2–TiO_2 before and after inert gas treatment. Peaks are located at the same points as in references JCPDS file of α-Fe_2O_3 (JCPDS no. 33-0664), SnO_2 (JCPDS no. 41-1445), and TiO_2 (JCPDS no. 21-1272). As the thickness of the hematite layer was ca. 300 nm, the metal oxide overlayer thickness was <100 nm, and because of the low treatment temperature of 500 °C, the peaks of Fe_2O_3/SnO_2–TiO_2 films appeared relatively weak. After inert gas treatment, the peaks of Fe_2O_3 appeared clearly stronger than before treatment because of the improvement of crystallinity. UV–vis spectroscopy shows that the absorption of these α-Fe_2O_3/SnO_2–TiO_2 photoanodes did not alter significantly after inert gas heat treatment (Figure 8S), indicating good stability and, in addition, no Fe_2TiO_5 or other mixed iron/metal oxide phases were found from our XRD and XPS studies, indicating that these were pure α-Fe_2O_3/SnO_2–TiO_2 films. Our results above demonstrated that under inert gas treatment at 500 °C, hematite undergoes a change in morphology. Plausibly, this allows for the overlayer dopants to diffuse into the Fe_2O_3 layer more readily.
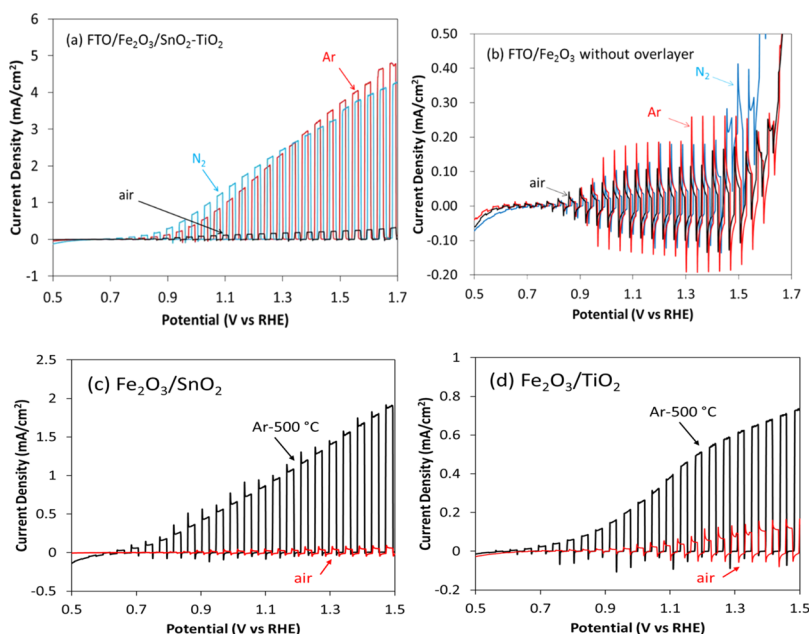
Figure 3. PEC response under chopped light: (a) α-Fe$_2$O$_3$/SnO$_2$–TiO$_2$ and (b) bare α-Fe$_2$O$_3$ films. (c) Fe$_2$O$_3$/SnO$_2$ and (d) Fe$_2$O$_3$/TiO$_2$ films before and after argon gas heat treatment. Air: before inert gas heat treatment. N$_2$: after treatment in nitrogen gas at 500 °C for 1 h. Ar: after treatment in argon gas at 500 °C for 1 h.

PEC performance of the α-Fe$_2$O$_3$/SnO$_2$–TiO$_2$ electrodes was investigated first by measuring the photocurrent density–potential (J–V) curves, as shown in Figure 3a. The α-Fe$_2$O$_3$/SnO$_2$–TiO$_2$ films were measured in 1 M NaOH (pH 13.6) electrolyte under 1 sun with an AM 1.5G filter. Without inert gas heat treatment (black line), the photocurrent was low (<0.6 mA/cm^2 at 1.7 V vs RHE). Astonishingly, after heating in nitrogen or argon gas at 500 °C, they exhibited a significant increase in activity to around 5.0 mA/cm^2 at 1.7 V versus RHE. The activity was recorded from the α-Fe$_2$O$_3$ containing both SnO$_2$ and TiO$_2$, with a photocurrent of ca. 2.0 mA/cm^2 at 1.23 V versus RHE. Furthermore, the onset potential exhibited a dramatic cathodic shift by as much as 0.7 V versus RHE. Generally speaking, onset potential can be improved by surface treatment. On the other hand, photocurrent plateau can be improved by increase in charge carrier concentration via doping.[5,16,24] To compare the effect of heat treatment in argon versus nitrogen, J–V curves were collected from α-Fe$_2$O$_3$/SnO$_2$–TiO$_2$ films (Figure 3a). Interestingly, after N$_2$ treatment the photocurrent onset shifted cathodically to a greater extent than after Ar treatment. In the low potential range, the N$_2$-treated samples showed higher photocurrent density (1.04 mA/cm^2 at 1.0 V vs RHE) than the Ar-treated samples (0.64 mA/cm^2 at 1.0 V vs RHE). On the other hand, in the high potential range, the Ar-treated samples showed higher photocurrent density than the N$_2$-treated samples (J_{Ar} = 3.32 mA/cm^2 at 1.5 V vs RHE, J_{N_2} = 2.71 mA/cm^2 at 1.5 V vs RHE). Similar relationship between Ar and N$_2$ treatment was obtained from the J–V curves of the α-Fe$_2$O$_3$/SnO$_2$–TiO$_2$ samples processed after annealing at 450 °C (Figure 9S). It is generally accepted that the conductivity of hematite and the amount of band bending both affect the photocurrent at higher potentials, whereas the onset potential shift is controlled by surface state passivation.[5,16,24] However, in previous literatures, the onset potential was in the range of 0.8–1.0 V versus RHE. In this study, the onset potential of α-Fe$_2$O$_3$/SnO$_2$–TiO$_2$ (inert gas) films showed more negative values at 0.65 V versus

RHE (Figure 10Sa,b). Even though the onset potential of N$_2$-treated Fe$_2$O$_3$/SnO$_2$–TiO$_2$ and Ar-treated Fe$_2$O$_3$/SnO$_2$–TiO$_2$ are the same at 0.65 V versus RHE, the photocurrent density has noticeable difference in the low potential range. Likely if onset potential is in a high level, it will be difficult to shift any further. The surface state effect may only display on photocurrent in the low potential range. The difference in the effect of Ar and N$_2$ treatment on the photocurrent is dominated by the morphological change from heating hematite in a low oxygen atmosphere. This suggests that nitrogen treatment has a greater effect on the surface of hematite, whereas argon heat treatment permits SnO$_2$–TiO$_2$ migration into the bulk. Both gases have a different level of oxygen impurity—this gives a different partial pressure of oxygen and this has the greatest effect on the results. From the SEM/EDS, XRD, and PEC results, it is likely that the SnO$_2$–TiO$_2$ overlayer can diffuse deeper into the hematite host after argon heat treatment compared to nitrogen, leading to higher photocurrent plateau. In addition, PEC performances of individual SnO$_2$ and TiO$_2$ overlayers on α-Fe$_2$O$_3$ were measured (Figure 3c,d). The photocurrent density after heating at 500 °C in argon increased; for example, in the case of α-Fe$_2$O$_3$/SnO$_2$ film, the photocurrent density went up from 0.08 to 1.20 mA/cm^2 at 1.23 V versus RHE. However, the maximum photocurrent was not as high compared to the composite SnO$_2$–TiO$_2$ on α-Fe$_2$O$_3$ photoanode. Furthermore, little change in PEC performance was exhibited by the pure α-Fe$_2$O$_3$ film after inert gas treatment (Figure 3b). This indicates that the excellent photoactivity is a result of the presence of the SnO$_2$–TiO$_2$ overlayer. From the results above, the migration of the nanosized metal oxide species from the overlayer into the α-Fe$_2$O$_3$ layer appears to occur more readily after inert gas treatment than after heat treatment in air, and therefore leads to a certain amount of doping at the interface of the hematite surface.

To experimentally ascertain the effect of Sn/Ti doping on the electronic properties of hematite, donor densities (N_A) and
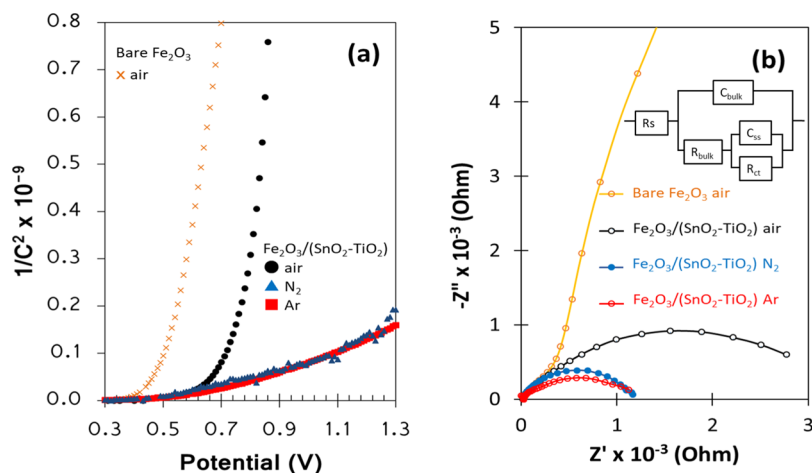
Figure 4. (a) Mott−Schottky plot of bare $Fe_2O_3/SnO_2−TiO_2$ electrode after annealing in air, argon, and nitrogen gas at 500 °C for 1 h. (b) Nyquist plots of bare Fe_2O_3 and $Fe_2O_3/SnO_2−TiO_2$ in air, nitrogen, and argon gas at 500 °C for 1 h treated films, data collected at a bias of 1.23 V vs RHE under 1 sun AM 1.5G simulated light in a 1 M NaOH aqueous solution.

flat-band potentials (V_{fb}) of the α-Fe_2O_3/MO anodes were estimated from the Mott−Schottky plot (Figures 4a and 11Sa−c). From the Mott−Schottky plot of before and after inert gas treatment, the slope of the linear part of the curves understandably presented a difference. The summary of the Mott−Schottky plot analysis is shown in Tables 1 and 2. The

Table 1. Flat Band Potential (V_{fb}) and Carrier Density (N_A) of $Fe_2O_3/SnO_2−TiO_2$ Films Were Obtained from the Mott−Schottky Plot of Figure 11Sa,b[a]

		V_{fb} (V vs RHE)	N_A (cm^{-3})
Fe_2O_3	air	0.55	6×10^{18}
	Ar	0.61	6×10^{18}
	N_2	0.62	5×10^{18}
$Fe_2O_3/SnO_2−TiO_2$	air	0.88	2×10^{18}
	Ar	0.69	3×10^{20}
	N_2	0.61	3×10^{20}

[a]Air: before inert gas heat treatment, Ar: after annealing in argon gas at 500 °C for 1 h, N_2: after annealing in nitrogen gas at 500 °C for 1 h.

Table 2. Flat Band Potential (V_{fb}) and Carrier Density (N_A) of $Fe_2O_3/SnO_2−TiO_2$ Films Were Counted from Mott−Schottky Plot of Figure 11Sc[a]

	V_{fb} (V vs RHE)	N_A (cm^{-3})
Fe_2O_3	0.61	6×10^{18}
Fe_2O_3/TiO_2	0.63	2×10^{19}
Fe_2O_3/SnO_2	0.70	3×10^{20}
$Fe_2O_3/SnO_2−TiO_2$	0.69	3×10^{20}

[a]Data were collected after annealing in argon gas at 500 °C for 1 h.

flat-band potentials are consistent and matched to onset potentials of bare α-Fe_2O_3 (air) and α-$Fe_2O_3/SnO_2−TiO_2$ (inert gas) films showing at ca. 0.55 V versus RHE and ca. 0.65 V versus RHE, respectively (Figures 3a,b and 10Sa−c). At a low temperature of <500 °C, heat treatment for hematite has been discussed previously[22] in which there is no significant change in the flat-band potential. In Table 1, the flat-band position and donor density almost did not change after heat treatment of the bare Fe_2O_3 films (V_{fb} = ~0.6 V vs RHE and N_A = ~10^{18} cm^{-3}), so there was no resultant change in

photoresponse. In contrast, it is clear that the flat-band potential of $Fe_2O_3/SnO_2−TiO_2$ (air) shifted to more positive values, possibly due to the influence of the metal oxide overlayer. It was considered that because the dopants were not incorporated into hematite sufficiently, there was no change in the donor density. However, after inert gas heat treatment, the donor densities of the films were of the order of 10^{18} cm^{-3} for Fe_2O_3 and up to 10^{20} cm^{-3} for α-$Fe_2O_3/SnO_2−TiO_2$. A higher donor density can lead to an increase in electrical conductivity.[20] The interfacial properties between the hematite photoelectrode and the electrolyte were also analyzed by electrochemical impedance spectroscopy (EIS) measurements. The inset figure of Figure 4b shows the electronic equivalent circuit model representing the hematite photoanode/electrolyte system used in the EIS data modeling. R_S represents the circuit series resistance, whereas R_{bulk} and R_{ct} represent the resistance of the bulk charge-trapping resistance and charge-transfer resistance across the hematite−electrolyte interface, respectively. C_{bulk} represents the bulk capacitance of space-charge layer and the Helmholtz layer. C_{ss} represents the capacitance corresponding to surface states. The Nyquist plots (imaginary-real components of impedance plots, $-Z''$ vs Z') were collected at 1.23 V versus RHE under 1 sun light; it is obvious from Figure 4b that the maximum imaginary impedance ($-Z''$) of inert gas-treated $Fe_2O_3/SnO_2−TiO_2$ films are less than 0.5×10^3 Ω. The maximum imaginary impedance of the $Fe_2O_3/SnO_2−TiO_2$ (air) electrode without inert gas treatment showed a higher number of ca. 1×10^3 Ω. Simultaneously, the bare Fe_2O_3 (air) electrode exhibited a much larger maximum imaginary impedance of ca. 10×10^3 Ω. Inert gas treatment is thought to be able to promote the conductivity of the hematite anode by charge separation and charge transport properties. As a result, the recombination rate of electron−hole pairs was decreased and the photocurrent density was improved. Many literatures have been investigated for Sn and Ti doped into hematite. It is interpreted that the transportation of electrons is improved by creating a heterojunction of the suitable position of the conduction bands.[20,27,28] Therefore, an increase in electrical conductivity can lead to longer lifetime of photogenerated charge carriers from the consequence of reduced recombination. On the other hand, according to the Dunn et al. report,[25] doping Sn into

hematite can accelerate the hole transfer rate in hematite. From our results of PEC measurements, both separation of charge carriers in hematite and transfer of holes across the anode as well as the electrolyte interface have been promoted by doping Sn and Ti into hematite under inert gas at <500 °C.

We carried out photoluminescence (PL) measurements (Figure 12S) on the α-Fe$_2$O$_3$/SnO$_2$–TiO$_2$ samples. We observed strong emissions from the sample before inert gas treatment, which was the PL response exhibited at about 570 nm, which can be assigned to band edge emission. Obviously, the samples after Ar and N$_2$ treatment resulted in a significant decrease in the emission intensity, which is a strong indication of the efficiency of charge separation. This is in good agreement with our PEC observation. High donor density and low PL intensity suggested the SnO$_2$–TiO$_2$ overlayer after inert gas treatment can improve electron transfer through an increase in charge conductivity, and therefore can reduce electron–hole recombination. Indeed, dopants such as Sn and Ti have been reported to improve photoactivity by increasing the donor density, carrier conductivity, and charge separation, along with decreasing the density of trap states and electron–hole recombination.[13,20,26−29] The nanohybrid metal oxide SnO$_2$–TiO$_2$, in effect, creates suitable junctions with hematite for photogenerated electron transfer from the metal oxides into hematite and through to the counter electrode. Consequently, by applying a low bias, the holes diffuse to the surface to promote water oxidation.[28] To confirm that the photocurrent was indeed a direct product of water splitting as opposed to side reactions, the photogenerated amounts of hydrogen and oxygen were measured by gas chromatography, while applying a constant potential of 1.5 V versus RHE. Evolution of hydrogen and oxygen from a α-Fe$_2$O$_3$/SnO$_2$–TiO$_2$ hybrid anode were collected at regular intervals. After 90 min reaction, 100 μmol of hydrogen and 51 μmol of oxygen were measured from the headspace, equivalent to an approximate 2:1 molar ratio (Figure 5). This indicates that the photocurrent is a direct
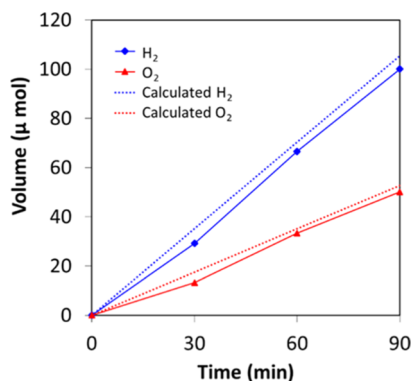

Figure 5. Gas evolution of hydrogen and oxygen from the Fe$_2$O$_3$/SnO$_2$–TiO$_2$ anode measured by gas chromatography (GC). The dotted lines are the amount of H$_2$ (blue) and O$_2$ (red) calculated from the photocurrent.

result of water splitting. Furthermore, the faradic efficiency was over 90%. This result indicated that with the applied bias at 1.5 V versus RHE, the photogenerated holes can move from the valence band of hematite to the electrolyte, passing through the remaining ultrathin overlayer for water oxidation. The stability test revealed an excellent record for α-Fe$_2$O$_3$/SnO$_2$–TiO$_2$ (Figure 6); the slight decrease in photocurrent is due to the accumulation of oxygen gas bubbles on the surface.
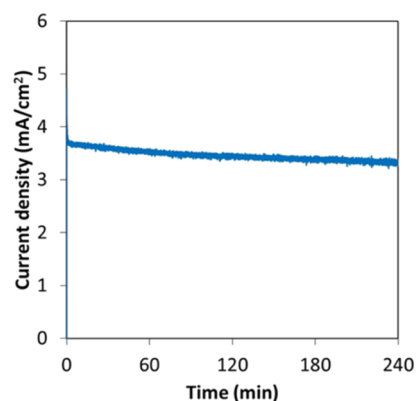

Figure 6. Stability test of the Fe$_2$O$_3$/SnO$_2$–TiO$_2$ photoanode under an applied potential of 1.5 V vs RHE.

With the intent to investigate the effect of air/inert gas heat treatment and metal oxide incorporation on the electronic properties of hematite, DFT modeling of Fe$_2$O$_3$ was undertaken in parallel with the experimental work. To elucidate the effects of doping in the bulk and on the {0001} surface, the Perdew−Burke−Ernzerhof (PBEsol) + U[30−32] approach was utilized to calculate large supercells and slabs to simulate the dilute limit. PBEsol + U is known to accurately describe the structural and electronic properties of Fe$_2$O$_3$ compared to an experiment.[33−37] The substitutional dopants considered in this study were Ti and Sn to mimic the effects of unintentional incorporation of dopants from the TiO$_2$ and SnO$_2$ overlayers, respectively.

The conventional unit cell of α-Fe$_2$O$_3$ is shown in Figure 13S, displaying the crystal structure of the three-dimensional array of the FeO$_6$ distorted octahedra. The structural parameters and bond lengths are shown in Table 2S and show excellent agreement with experimentally measured values and with previous theoretical works using DFT + U.[33−37]

The density of states (DOS) and band structure for bulk α-Fe$_2$O$_3$ are shown in Figures 14Sa,b, respectively. In the DOS, the valence-band maximum (VBM) is primarily made up of ~70% O 2p states mixing with ~30% Fe 3d states, whereas the conduction-band minimum (CBM) is predominantly Fe 3d states (~90%) with some mixing with O 2p states (~10%). The band structure in Figure 14Sb shows that α-Fe$_2$O$_3$ has an indirect band gap of ~2.19 eV with a VBM situated between Γ and L and the CBM at F, which is consistent with previous theory and experiment.[33−35,38−43] The direct band gap from the VBM to the conduction band has a magnitude of ~2.29 eV. Both the VBM and CBM are made up of flat bands with high effective masses. The reasoning behind this is the lack of mixing between Fe and O at either the VBM or CBM. This is in contrast to the energy range >5 eV, which shows increased dispersion due to an enhanced mixing between the Fe s states and O p states. The dopant states were calculated using oxygen partial pressures to simulate the experimental conditions of 773 K, 1 atm. Substitutional Sn and Ti dopant defects (Sn$_{Fe}$ and Ti$_{Fe}$) possess formation enthalpies of 3.32 and 2.73 eV, respectively, suggesting easy incorporation of Sn and Ti into the Fe$_2$O$_3$ lattice under thermodynamic equilibrium. This is corroborated with previous theoretical studies showing similar low formation energies.[33,44] The DOS for the bulk supercells are shown in Figure 7a−c for the pure, Ti-, and Sn-doped supercells. For Ti$_{Fe}$ (Figure 7b), the Ti d states appear at the CBM and continue to be prevalent in the conduction band up
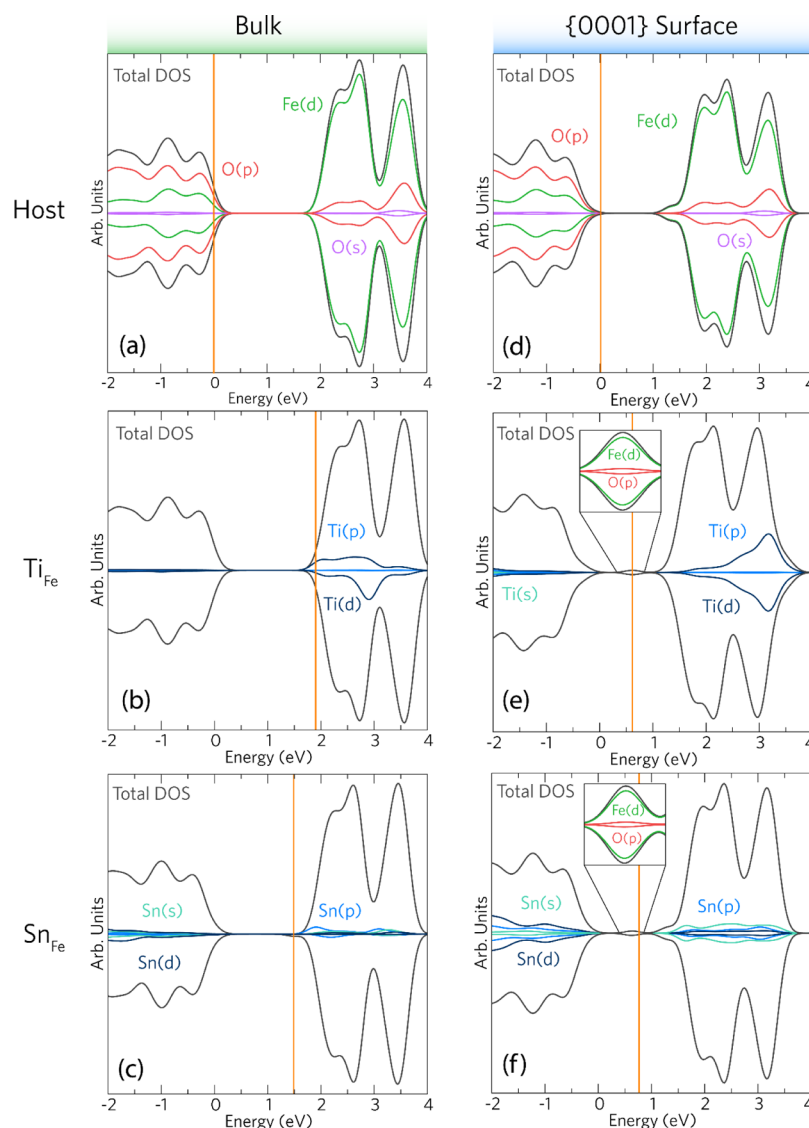
Figure 7. The dopant states DOS for the bulk and {0001} surfaces of α-Fe$_2$O$_3$. (a−c) correspond to the host, Ti-, and Sn-doped supercells respectively. (d−f) show the DOS for the {0001} surfaces of the host, Ti (site 1), and Sn (site 3) surfaces, respectively. In each example, the VBM is set to 0 eV and the position of the Fermi level is depicted by the orange line. Both spin-up and spin-down states are shown, and the dopant states have been scaled accordingly for clarity. In (e,f), the zoomed-in gap states are inset.

to ∼4 eV. This behavior is seen in other theoretical works using DFT + U.[45] The Fermi level in Ti-doped Fe$_2$O$_3$ appears at ∼1.94 eV compared to the band gap in the host supercell of ∼2.1 eV. The DOS for the Sn-doped supercell shows a considerable percentage of Sn d and s states in the valence band from ∼2 to ∼1 eV; there is also substantial Sn s and p states from the CBM toward 4 eV. The Fermi level occurs at ∼1.5 eV above the VBM indicating a large reduction of the band gap from the host supercell. The formation energies for the {0001} surface are calculated at 773 K, 1 atm and are shown in Table 3S. Sn$_{Fe}$ is found to be most stable in site 3 (Figure 15S) on the {0001} surface and is more stable than the next most preferable site (site 1) by ∼0.26 eV (ΔH_f = 0.72 eV). Ti$_{Fe}$, on the other hand, is shown to be most stable in site 1, which is the three-coordinate position and is more stable than site 2 by ∼0.14 eV (ΔH_f = 0.14 eV). From our calculations, surface doping is therefore highly favorable in Fe$_2$O$_3$, predicting a large concentration of dopant species at the interface. The DOS for the pure {0001} surface, Ti-doped

surface (in site 1), and the Sn-doped surface (in site 3) are shown in Figure 7d−f. For both doped surfaces, there exist gap states ∼0.6 eV above the VBM comprising predominantly Fe d hybridization with O p. In each case, the Fermi level on the surface is trapped in these states at ∼0.6 and ∼0.76 eV above the VBM for Ti$_{Fe}$ and Sn$_{Fe}$, respectively. In Ti$_{Fe}$, most of the Ti d states occur in the conduction band from ∼2 to 4 eV above the VBM. In the Sn-doped {0001} surface, there is considerable mixing of Sn s and d states in the valence band up to the VBM owing to the possibility of Sn^{2+} lone pairs, while substantial Sn s, p, and d states are seen in the conduction band. Our results indicate that the dopant states (not water-splitting reaction mechanism) will be most prominent at the α-Fe$_2$O$_3$/SnO$_2$(TiO$_2$) interfaces and should explain the enhanced photocatalytic activity seen. Both Ti and Sn dopants are low formation energy donors and have been known to increase the conductivities of Fe$_2$O$_3$ films, which has the effect of enhancing the electron transfer from the conduction band of Fe$_2$O$_3$ to the SnO$_2$ (TiO$_2$) layers.[46]

CONCLUSIONS

In summary, we developed a series of highly active, stable α-Fe_2O_3 photoelectrodes for PEC water splitting, whose activity was remarkably enhanced through addition of a metal oxide overlayer and low heat ($\leq$500 °C) treatment under an inert gas. This method of overlayer formation is much simpler and lower in cost than other thin film deposition techniques, such as ALD, and therefore is easier to scale-up. Using this method, the average unit cell volume decreased (calculated from lattice parameters of Fe_2O_3/TiO_2 and Fe_2O_3/SnO_2), and the morphology changed significantly after heating in argon gas. We have shown that the SnO_2–TiO_2 layer after inert gas treatment induces a substantial effect on the PEC activity of hematite, both in terms of maximum photocurrent and onset potential. We found that the metal oxide dopants can migrate easily from the overlayer through to the α-Fe_2O_3 layer at modest temperatures under reduced oxygen conditions, which ultimately led to a 10-fold rise in photocurrent. From our electrochemical measurements, it was found that the donor densities of the films increased when Sn and Ti dopants are incorporated. Theoretical modeling revealed that the dopant defects, Ti_{Fe} and Sn_{Fe}, were found to possess low formation energies under the experimental synthesis conditions. More likely, under inert gas treatment, even at low temperatures ($\leq$500 °C), intrinsic electronic structure of hematite can be improved by Ti_{Fe} and Sn_{Fe}. This will, in turn, lead to improved donor density and electronic conductivity and retard recombination, therefore, higher stable photocurrents can be obtained. We believe this facile, cost-effective strategy can be applied to other hematite/dopant photoelectrodes to strengthen their activity for solar fuel production.

EXPERIMENTAL SECTION

Film Preparation. Nanoparticle α-Fe_2O_3 films (area of about 1.0 cm × 1.5 cm) were fabricated by galvanostatic deposition at 60 °C. The bath was an aqueous solution containing 0.2 M iron(II) chloride tetrahydrate ($FeCl_2\cdot4H_2O$, Acros Organics). Conducting FTO glass (TEC15, NSG) was used as the substrate. Before deposition, the FTO glass substrates were sonicated in acetone and distilled water for 30 min each, dried in air, and then placed in a furnace at 400 °C for 30 min. The anodic deposition was carried out in galvanostatic mode. A 5 cm² Pt gauze was used as the counter electrode. Iron oxyhydroxide (FeOOH) films were deposited at a constant current density of +0.3 mA/cm², corresponding to an electric charge of 0.27 C/cm². After each deposition, the resulting film was rinsed with deionized water and dried in air. To obtain crystalline α-Fe_2O_3 electrodes, as-deposited films were annealed in air at 500 °C for 1 h at a rate of 5 °C/min. Titanium dioxide (TiO_2) and tin oxide (SnO_2) were introduced as overlayers on the α-Fe_2O_3 films. The precursor of TiO_2 was 0.01 wt % peroxotitanic acid, prepared by dissolving amorphous TiO_2 into hydrogen peroxide (H_2O_2, Sigma-Aldrich, 30 wt % in H_2O) in an ice-bath. The SnO_2 precursor solution was obtained from a filtered solution of 0.05 g tin powder (Sn, 150 μm, Goodfellow Ltd, England) in 20 ml H_2O_2, after stirring for 24 h. The precursor mixture was made by adding the SnO_2 precursor solution to the peroxotitanic acid of 1:1 vol %. The solution was sonicated for 10 min before spin-coating onto the α-Fe_2O_3 film at 1000 rpm for 10 s. This coating process was repeated five times to obtain the overlayer thickness of 100 nm, followed by heat treatment at 500 °C in

air for 1 h. A final annealing process was carried out at 450, 500, and 550 °C, ramp rate 5 °C/min for 1 h in nitrogen (BOC, 99.998%) or argon gas (BOC, 99.998%), flow rate 200 mL/min.

Film Characterization. The morphologies of the films were characterized using a JEOL JSM-6700F field emission SEM. The EDS analysis result was obtained by a FIB-SEM (Zeiss Crossbeam 540) equipped with an EDS unit (Oxford Instruments, silicon drift detector—X-Max^N). The acceleration voltage was 15 kV. XPS data were collected on a Thermo Scientific K-Alpha X-ray photoelectron spectrometer under ultrahigh vacuum ($<5 \times 10^8$ Torr) using a monochromatic Al Kα X-ray source, at an operating ion gun energy of 200 eV, scanning 10 times for each element. The adventitious carbon 1s peak was calibrated to 284.5 eV and used as an internal standard to compensate for any charging effects. Phase identification of the films was achieved using a Bruker D8 DISCOVER LynxEye thin-film X-ray diffractometer equipped with Cu Kα1 (using 40 kV and 40 mA, λ = 1.540619 Å) radiation, operated in 2θ scan mode from 15° to 66°, X-ray incident angle at 1°, 0.05° step size, 6 s per step. To confirm α-Fe_2O_3, SnO_2, and TiO_2, reference JCPDS files for α-Fe_2O_3 (JCPDS no. 33-0664), SnO_2 (JCPDS no. 41-1445), and TiO_2 (JCPDS no. 21-1272) are cited. The PL spectra were obtained by using Horiba Scientific LabRAM HR Evolution as the excitation source operated at a wavelength of 325 nm.

PEC Measurements. Photoresponse of the α-Fe_2O_3 films was measured using a 150 W xenon solar simulator lamp (Newport, 96000) fitted with an AM 1.5G filter, a monochromator with a 395 nm long pass filter, and a home built programmable light chopper (Oriental Motor). The light output was calibrated to 1 sun (100 mW/cm²). PEC performance of the films was evaluated in a three-electrode configuration using a potentiostat/galvanostat analyzer (Ivium Technologies GmBH). The reference electrode was Ag/AgCl in 3 M KCl (BaSi Inc., UK), and a 5 cm² Pt gauze was used as the counter electrode. Films were illuminated from the FTO glass substrate side. The scan rate for cyclic voltammetry was 10 mV/s. The electrolyte comprised a 1 M NaOH solution (pH 13.6). All potentials in this work are reported against the RHE, obtained from those relative to the Ag/AgCl reference electrode using the Nernst equation, $E_{RHE} = E^0_{Ag/AgCl} + E_{Ag/AgCl} + 0.059$ pH, where E_{RHE} is the converted potential versus RHE, $E^0_{Ag/AgCl}$ = 0.1976 at 25 °C, and $E_{Ag/AgCl}$ is the experimentally measured potential against the Ag/AgCl reference. Mott–Schottky plots (capacitance–potential curves) were recorded of the impedance in the dark at a frequency of 10 k Hz with ac amplitude of 10 mV. Equation 1 was used to determine the flat-band potential (V_{fb}) and carrier density (N_A).

$$\frac{1}{C^2} = \frac{2}{\varepsilon_0\varepsilon_r e N_A}\left(V - V_{fb} - \frac{k_B T}{e}\right) \tag{1}$$

where N_A is the carrier density, ε_0 is the permittivity in vacuum, ε_r is the relative permittivity (α-Fe_2O_3 was taken as 32),[47] V is the applied potential, T is the absolute temperature, e is the electronic charge, and k_B is the Boltzmann constant. EIS data were recorded using a Zennium E Electrochemical Workstation (Zahner) under solar simulator light (1 sun, AM 1.5G) with a 100 kHz to 100 mHz frequency range at 0.23 V versus Ag/AgCl in the electrolyte of 1 M NaOH solution (pH 13.6) and with an alternate current perturbation of 10 mV.

GC Measurements. PEC water splitting on the Fe_2O_3/SnO_2–TiO_2 film was carried out at an applied potential of 1.5 V versus RHE under AM 1.5G 100 mW/cm^2 irradiation. An airtight three-electrode configuration electrochemical cell was used, and 1 M NaOH (pH 13.6) was used as an electrolyte. The evolved gases during the reaction were collected by a gas-tight syringe from the headspace of the cell at regular intervals. The evolved hydrogen and oxygen amounts were recorded by gas chromatography (Varian 430-GC, 5A mol. sieve column, TCD detector, oven at 50 °C, Ar gas as a carrier gas at a flow rate of 10 mL/min).

Computational Methodology. To simulate the bulk and surface properties of α-Fe_2O_3, the periodic DFT code VASP[48−51] together with the PBEsol[52−54] functional was used. The PBEsol functional is a gradient corrected functional revised for solids and gives a reasonable representation of the structural and electronic parameters of inorganic semiconductor materials, despite the well-documented underestimation of the band gap.[52,55,56] An on-site Coulomb "U" correction[57] was applied (U_{eff} = 4 eV) to describe the Fe d states, consistent with previous theoretical studies.[33,34,38,58,59] The projector augmented wave method[60] was used to describe the interactions between the core and valence electrons for each species involved in the calculations (Fe[Ar], O[He], Ti[Ar], and Sn[Kr]).

The calculations were split into the bulk structural and electronic properties, bulk dopant states, and surface dopant states. For the bulk properties, a geometry optimization was carried out on the unit cell of α-Fe_2O_3 containing 10 atoms which crystallizes in the rhombohedral $R\bar{3}c$ space group (corundum). For all optimizations (unit cell, supercells, and surface slabs), a plane-wave energy cutoff of 700 eV was used for accurate total energy convergence, which was deemed to be complete when the force on all atoms was less than 0.01 eV Å^{-1}. The unit cell was sampled using a Γ-centered k-point grid of $8 \times 8 \times 8$. From our calculations, the lowest energy magnetic ordering was determined to be antiferromagnetic as seen in neutron diffraction studies and previous DFT work.[35,38,61−63]

To elucidate the effects of doping in the bulk, large $3 \times 3 \times 3$ supercells containing 270 atoms were created to simulate the dilute limit. Structural optimizations were carried out relaxing all but the cell volume and angles using a Γ-centered k-point grid of $2 \times 2 \times 2$. The substitutional dopants considered in this study were Ti and Sn to mimic the effects of unintentional incorporation of dopants from the TiO_2 and SnO_2 interfaces, respectively. The enthalpy of formation of the defects was treated using the equation

$$\Delta H_f(D) = (E^D - E^H) + \sum_i n(E_i + \mu_i) \qquad (2)$$

E^D and E^H refer to the total energies of the defective supercell in the neutral charge state and the host supercells, respectively. E_i and μ_i are the elemental reference energies in their standard states (where i = $Fe_{(s)}$, $O_{2(g)}$, $Ti_{(s)}$ and $Sn_{(s)}$) and their respective chemical potentials, respectively. n refers to the number of atoms of i taken away from ($+n$) or added to ($-n$) the system.

To gain an insight into surface segregation, the formation energies for Ti and Sn doping were calculated on the most stable Fe-terminated {0001} surface of α-Fe_2O_3.[58,59,64,65] To cleave the surface, the Metadise code[66] was used to yield a 260-atom surface with a ~27 Å thick slab with ~27 Å of vacuum. On the {0001} surface, three different Fe sites are seen (depicted in Figure 15Sa,b). Site 1 has a three-coordinate trigonal pyramid coordination, with sites 2 and 3 possessing distorted octahedral coordination. Γ-centered k-point grids of $3 \times 3 \times 1$ were used to ensure adequate convergence of the total energy when optimizing the surfaces. Doping was carried out on both sides of the slab to ensure that no dipole moment perpendicular to the surface was created.

The chemical potential of μ_O can be calculated using the oxygen partial pressure and temperature using the equation[67]

$$\mu_O(T, p^0) = \frac{1}{2}[H(T, p^0, O_2) - H(0\,K, p^0, O_2)]$$
$$- \frac{1}{2}T[S(T, p^0, O_2) - S(0\,K, p^0, O_2)]$$

where H, T, and S are enthalpy, temperature, and entropy, respectively. p^0 = 1 atm with reference to a zero state; $\mu_O(0\,K, p^0) = \frac{1}{2}E_{O_2}^{total} = 0$.[68−70] In the experimental synthesis, annealing of the layered films occurred at 500 °C (~773 K) and 1 atm, thus μ_O (773 K, 1 atm) = −0.82 eV, determined using data from thermochemical tables.[71] μ_{Fe} (773 K, 1 atm) can, therefore, be determined within the formation enthalpy of Fe_2O_3 giving μ_{Fe} (773 K, 1 atm) = −3.43 eV. μ_{Ti} and μ_{Sn} are limited via the formation of the secondary phases, TiO_2 and SnO_2, respectively. SnO_2 and TiO_2 were relaxed using plane-wave cutoffs of 700 eV and Γ-centered k-point meshes of $8 \times 8 \times 8$ (FeO) and $8 \times 8 \times 6$ (SnO_2 and TiO_2) with the same force convergence criterion mentioned above. The enthalpies of formation for each phase was determined to be −3.32 eV (FeO), −5.36 eV (SnO_2), and −9.06 eV (TiO_2), which agree well with the experiment.[71] μ_{Ti} (773 K, 1 atm) and μ_{Sn} (773 K, 1 atm) are thus calculated to be −7.66 eV and −3.66 eV, respectively.

■ ASSOCIATED CONTENT

Ⓢ Supporting Information

The Supporting Information is available free of charge on the ACS Publications website at DOI: 10.1021/acsomega.8b02444.

> The results of the XPS and FIB-SEM/EDS spectra, XRD patterns, UV−vis spectrum, lattice parameters calculation, photocurrent-potential curves, PEC characterization, Mott−Schottky plots, PL spectrum, crystal structure of α-Fe_2O_3, calculated DOS and band structure, (PBEsol + U) and experimental bond lengths and lattice parameters for α-Fe_2O_3, and {0001} surface of α-Fe_2O_3 (PDF)

■ AUTHOR INFORMATION

Corresponding Authors
*E-mail: socmanho@um.edu.mo (S.H.-K.).
*E-mail: i.p.parkin@ucl.ac.uk (I.P.P.).

ORCID ⓘ

SocMan Ho-Kimura: 0000-0003-2284-707X
Benjamin A. D. Williamson: 0000-0002-6242-1121
Sanjayan Sathasivam: 0000-0002-5206-9558
Wenjun Luo: 0000-0001-6760-6929
David O. Scanlon: 0000-0001-9174-8601
Junwang Tang: 0000-0002-2323-5510

■ REFERENCES

(1) Murphy, A. B.; Barnes, P. R. F.; Randeniya, L. K.; Plumb, I. C.; Grey, I. E.; Horne, M. D.; Glasscock, J. A. Efficiency of solar water splitting using semiconductor electrodes. *Int. J. Hydrogen Energy* **2006**, *31*, 1999−2017.

(2) Brillet, J.; Grätzel, M.; Sivula, K. Decoupling Feature Size and Functionality in Solution-Processed, Porous Hematite Electrodes for Solar Water Splitting. *Nano Lett.* **2010**, *10*, 4155−4160.

(3) Kim, J. Y.; Magesh, G.; Youn, D. H.; Jang, J.-W.; Kubota, J.; Domen, K.; Lee, J. S. Single-crystalline, wormlike hematite photoanodes for efficient solar water splitting. *Sci. Rep.* **2013**, *3*, 2681.

(4) Kennedy, J. H.; Frese, K. W., Jr. Photooxidation of Water at α-Fe$_2$O$_3$ Electrodes. *J. Electrochem. Soc.* **1978**, *125*, 709−714.

(5) Steier, L.; Herraiz-Cardona, I.; Gimenez, S.; Fabregat-Santiago, F.; Bisquert, J.; Tilley, S. D.; Grätzel, M. Understanding the Role of Underlayers and Overlayers in Thin Film Hematite Photoanodes. *Adv. Funct. Mater.* **2014**, *24*, 7681−7688.

(6) Tilley, S. D.; Cornuz, M.; Sivula, K.; Grätzel, M. Light-induced water splitting with hematite: improved nanostructure and iridium oxide catalysis. *Angew. Chem., Int. Ed.* **2010**, *49*, 6405−6408.

(7) Sivula, K.; Zboril, R.; Le Formal, F.; Robert, R.; Weidenkaff, A.; Tucek, J.; Frydrych, J.; Grätzel, M. Photoelectrochemical Water Splitting with Mesoporous Hematite Prepared by a Solution-Based Colloidal Approach. *J. Am. Chem. Soc.* **2010**, *132*, 7436−7444.

(8) Kay, A.; Cesar, I.; Grätzel, M. New Benchmark for Water Photooxidation by Nanostructured α-Fe2O3Films. *J. Am. Chem. Soc.* **2006**, *128*, 15714−15721.

(9) Kleiman-Shwarsctein, A.; Huda, M. N.; Walsh, A.; Yan, Y.; Stucky, G. D.; Hu, Y.-S.; Al-Jassim, M. M.; McFarland, E. W. Electrodeposited Aluminum-Doped α-Fe$_2$O$_3$ Photoelectrodes: Experiment and Theory. *Chem. Mater.* **2010**, *22*, 510−517.

(10) Gurudayal; Chiam, S. Y.; Kumar, M. H.; Bassi, P. S.; Seng, H. L.; Barber, J.; Wong, L. H. Improving the Efficiency of Hematite Nanorods for Photoelectrochemical Water Splitting by Doping with Manganese. *ACS Appl. Mater. Interfaces* **2014**, *6*, 5852−5859.

(11) Hu, Y.-S.; Kleiman-Shwarsctein, A.; Forman, A. J.; Hazen, D.; Park, J.-N.; McFarland, E. W. Pt-Doped α-Fe$_2$O$_3$ Thin Films Active for Photoelectrochemical Water Splitting. *Chem. Mater.* **2008**, *20*, 3803−3805.

(12) Kronawitter, C. X.; Zegkinoglou, I.; Shen, S.-H.; Liao, P.; Cho, I. S.; Zandi, O.; Liu, Y.-S.; Lashgari, K.; Westin, G.; Guo, J.-H.; Himpsel, F. J.; Carter, E. A.; Zheng, X. L.; Hamann, T. W.; Koel, B. E.; Mao, S. S.; Vayssieres, L. Titanium incorporation into hematite photoelectrodes: theoretical considerations and experimental observations. *Energy Environ. Sci.* **2014**, *7*, 3100−3121.

(13) Annamalai, A.; Shinde, P. S.; Subramanian, A.; Kim, J. Y.; Kim, J. H.; Choi, S. H.; Lee, J. S.; Jang, J. S. Bifunctional TiO$_2$ underlayer

for α-Fe$_2$O$_3$ nanorod based photoelectrochemical cells: enhanced interface and Ti^{4+} doping. *J. Mater. Chem. A* **2015**, *3*, 5007−5013.

(14) Bohn, C. D.; Agrawal, A. K.; Walter, E. C.; Vaudin, M. D.; Herzing, A. A.; Haney, P. M.; Talin, A. A.; Szalai, V. A. Effect of Tin Doping on α-Fe$_2$O$_3$ Photoanodes for Water Splitting. *J. Phys. Chem. C* **2012**, *116*, 15290−15296.

(15) Ling, Y.; Wang, G.; Wheeler, D. A.; Zhang, J. Z.; Li, Y. Sn-Doped Hematite Nanostructures for Photoelectrochemical Water Splitting. *Nano Lett.* **2011**, *11*, 2119−2125.

(16) Le Formal, F.; Tétreault, N.; Cornuz, M.; Moehl, T.; Grätzel, M.; Sivula, K. Passivating surface states on water splitting hematite photoanodes with alumina overlayers. *Chem. Sci.* **2011**, *2*, 737−743.

(17) Zandi, O.; Hamann, T. W. Enhanced Water Splitting Efficiency Through Selective Surface State Removal. *J. Phys. Chem. Lett.* **2014**, *5*, 1522−1526.

(18) Ho-Kimura, S.; Moniz, S. J. A.; Handoko, A. D.; Tang, J. Enhanced photoelectrochemical water splitting by nanostructured BiVO$_4$−TiO$_2$ composite electrodes. *J. Mater. Chem. A* **2014**, *2*, 3948−3953.

(19) Biesinger, M. C.; Payne, B. P.; Grosvenor, A. P.; Lau, L. W. M.; Gerson, A. R.; Smart, R. S. C. Resolving surface chemical states in XPS analysis of first row transition metals, oxides and hydroxides: Cr, Mn, Fe, Co and Ni. *Appl. Surf. Sci.* **2011**, *257*, 2717−2730.

(20) Hahn, N. T.; Mullins, C. B. Photoelectrochemical Performance of Nanostructured Ti- and Sn-Doped α-Fe$_2$O$_3$ Photoanodes. *Chem. Mater.* **2010**, *22*, 6474−6482.

(21) Ling, Y.; Wang, G.; Wheeler, D. A.; Zhang, J. Z.; Li, Y. Sn-Doped Hematite Nanostructures for Photoelectrochemical Water Splitting. *Nano Lett.* **2011**, *11*, 2119−2125.

(22) Bedoya-Lora, F. E.; Hankin, A.; Holmes-Gentle, I.; Regoutz, A.; Nania, M.; Payne, D. J.; Cabral, J. T.; Kelsall, G. H. Effects of low temperature annealing on the photo-electrochemical performance of tin-doped hematite photo-anodes. *Electrochim. Acta* **2017**, *251*, 1−11.

(23) Pailhé, N.; Wattiaux, A.; Gaudon, M.; Demourgues, A. Impact of structural features on pigment properties of α-Fe$_2$O$_3$ haematite. *J. Solid State Chem.* **2008**, *181*, 2697−2704.

(24) Bassi, P. S.; Gurudayal; Wong, L. H.; Barber, J. Iron based photoanodes for solar fuel production. *Phys. Chem. Chem. Phys.* **2014**, *16*, 11834−11842.

(25) Dunn, H. K.; Feckl, J. M.; Müller, A.; Fattakhova-Rohlfing, D.; Morehead, S. G.; Roos, J.; Peter, L. M.; Scheu, C.; Bein, T. Tin doping speeds up hole transfer during light-driven water oxidation at hematite photoanodes. *Phys. Chem. Chem. Phys.* **2014**, *16*, 24610−24620.

(26) Uchiyama, H.; Yukizawa, M.; Kozuka, H. Photoelectrochemical Properties of Fe$_2$O$_3$−SnO$_2$ Films Prepared by Sol−Gel Method. *J. Phys. Chem. C* **2011**, *115*, 7050−7055.

(27) Monllor-Satoca, D.; Bärtsch, M.; Fàbrega, C.; Genç, A.; Reinhard, S.; Andreu, T.; Arbiol, J.; Niederberger, M.; Morante, J. R. What do you do, titanium? Insight into the role of titanium oxide as a water oxidation promoter in hematite-based photoanodes. *Energy Environ. Sci.* **2015**, *8*, 3242−3254.

(28) Barreca, D.; Carraro, G.; Gasparotto, A.; Maccato, C.; Warwick, M. E. A.; Kaunisto, K.; Sada, C.; Turner, S.; Gönüllü, Y.; Ruoko, T.-P.; Borgese, L.; Bontempi, E.; Van Tendeloo, G.; Lemmetyinen, H.; Mathur, S. Water Splitting: Fe$_2$O$_3$−TiO$_2$ Nano-heterostructure Photoanodes for Highly Efficient Solar Water Oxidation. *Adv. Mater. Interfaces* **2015**, *2*, 1500313.

(29) Tsyganok, A.; Klotz, D.; Malviya, K. D.; Rothschild, A.; Grave, D. A. Different Roles of Fe$_{1-x}$Ni$_x$OOH Cocatalyst on Hematite (α-Fe$_2$O$_3$) Photoanodes with Different Dopants. *ACS Catal.* **2018**, *8*, 2754−2759.

(30) Csonka, G. I.; Perdew, J. P.; Ruzsinszky, A.; Philipsen, P. H. T.; Lebègue, S.; Paier, J.; Vydrov, O. A.; Ángyán, J. G. Assessing the Performance of Recent Density Functionals for Bulk Solids. *Phys. Rev. B: Condens. Matter Mater. Phys.* **2009**, *79*, 155107.

(31) Perdew, J. P.; Burke, K.; Ernzerhof, M. Generalized Gradient Approximation Made Simple. *Phys. Rev. Lett.* **1996**, *77*, 3865−3868.

(32) Perdew, J. P.; Ruzsinszky, A.; Csonka, I.; Vydrov, O. A.; Scuseria, G. E.; Constantin, L. A.; Zhou, X.; Burke, K. Restoring the Density-Gradient Expansion for Exchange in Solids and Surfaces. *Phys. Rev. Lett.* **2008**, *100*, 136406.

(33) Zhou, Z.; Huo, P.; Guo, L.; Prezhdo, O. V. Understanding Hematite Doping with Group IV Elements: A DFT+U Study. *J. Phys. Chem. C* **2015**, *119*, 26303−26310.

(34) Pan, H.; Meng, X.; Cai, J.; Li, S.; Qin, G. 4D Transition-Metal Doped Hematite for Enhancing Photoelectrochemical Activity: Theoretical Prediction and Experimental Confirmation. *RSC Adv.* **2015**, *5*, 19353−19361.

(35) Zhou, Z.; Shi, J.; Guo, L. A Comparative Study on Structural and Electronic Properties and Formation Energy of Bulk α-Fe$_2$O$_3$ Using First-Principles Calculations with Different Density Functionals. *Comput. Mater. Sci.* **2016**, *113*, 117−122.

(36) Catti, M.; Valerio, G.; Dovesi, R. Theoretical Study of Electronic, Magnetic, and Structural Properties of α-Fe$_2$O$_3$ (hematite). *Phys. Rev. B: Condens. Matter Mater. Phys.* **1995**, *51*, 7441−7450.

(37) Finger, L. W.; Hazen, R. M. Crystal Structure and Isothermal Compression of Fe$_2$O$_3$, Cr$_2$O$_3$, and V$_2$O$_3$ to 50 Kbars. *J. Appl. Phys.* **1980**, *51*, 5362−5367.

(38) Kleiman-Shwarsctein, A.; Huda, M. N.; Walsh, A.; Yan, Y.; Stucky, G. D.; Hu, Y.-S.; Al-Jassim, M. M.; McFarland, E. W. Electrodeposited Aluminum-Doped α-Fe$_2$O$_3$ Photoelectrodes: Experiment and Theory. *Chem. Mater.* **2010**, *22*, 510−517.

(39) Gilbert, B.; Frandsen, C.; Maxey, E. R.; Sherman, D. M. Band-Gap Measurements of Bulk and Nanoscale Hematite by Soft x-Ray Spectroscopy. *Phys. Rev. B: Condens. Matter Mater. Phys.* **2009**, *79*, 035108.

(40) Dare-Edwards, M. P.; Goodenough, J. B.; Hamnett, A.; Trevellick, P. R. Electrochemistry and Photoelectrochemistry of Iron(III) Oxide. *J. Chem. Soc., Faraday Trans. 1* **1983**, *79*, 2027.

(41) Upul Wijayantha, K. G.; Saremi-Yarahmadi, S.; Peter, L. M. Kinetics of Oxygen Evolution at α-Fe$_2$O$_3$ Photoanodes: A Study by Photoelectrochemical Impedance Spectroscopy. *Phys. Chem. Chem. Phys.* **2011**, *13*, 5264.

(42) Yan, Y.; Huda, M.; Walsh, a.; Wei, S.; Al-Jassim, M.; Turner, J.; Garland, R. Theory of Oxides for Photo-Electrochemical Hydrogen Production. *Hydrogen and Fuel Cells Program 2009 Annual Report*; U.S. Department of Energy, 2009; pp 208−211.

(43) Huda, M. N.; Walsh, A.; Yan, Y.; Wei, S.-H.; Al-Jassim, M. M. Electronic, Structural, and Magnetic Effects of 3d Transition Metals in Hematite. *J. Appl. Phys.* **2010**, *107*, 123712.

(44) Pan, H.; Meng, X.; Liu, D.; Li, S.; Qin, G. (Ti/Zr,N) Codoped Hematite for Enhancing the Photoelectrochemical Activity of Water Splitting. *Phys. Chem. Chem. Phys.* **2015**, *17*, 22179−22186.

(45) Meng, X. Y.; Qin, G. W.; Li, S.; Wen, X. H.; Ren, Y. P.; Pei, W. L.; Zuo, L. Enhanced Photoelectrochemical Activity for Cu and Ti Doped Hematite: The First Principles Calculations. *Appl. Phys. Lett.* **2011**, *98*, 112104.

(46) Jana, S.; Mondal, A. Fabrication of SnO$_2$ / α-Fe$_2$O$_3$, SnO$_2$ / α-Fe$_2$O$_3$ − PB Heterostructure Thin Films : Enhanced Photodegradation and Peroxide Sensing. *ACS Appl. Mater. Interfaces* **2014**, *6*, 15832−15840.

(47) Steier, L.; Herraiz-Cardona, I.; Gimenez, S.; Fabregat-Santiago, F.; Bisquert, J.; Tilley, S. D.; Grätzel, M. Understanding the Role of Underlayers and Overlayers in Thin Film Hematite Photoanodes. *Adv. Funct. Mater.* **2014**, *24*, 7681−7688.

(48) Kresse, G.; Hafner, J. Ab initiomolecular dynamics for liquid metals. *Phys. Rev. B: Condens. Matter Mater. Phys.* **1993**, *47*, 558−561.

(49) Kresse, G.; Hafner, J. Ab initiomolecular-dynamics simulation of the liquid-metal-amorphous-semiconductor transition in germanium. *Phys. Rev. B: Condens. Matter Mater. Phys.* **1994**, *49*, 14251−14269.

(50) Kresse, G.; Furthmüller, J. Efficiency of Ab-Initio Total Energy Calculations for Metals and Semiconductors Using a Plane-Wave Basis Set. *Comput. Mater. Sci.* **1996**, *6*, 15−50.

(51) Kresse, G.; Furthmüller, J. Efficient Iterative Schemes for Ab Initio Total-Energy Calculations Using a Plane-Wave Basis Set. *Phys. Rev. B: Condens. Matter Mater. Phys.* **1996**, *54*, 11169.

(52) Csonka, G. I.; Perdew, J. P.; Ruzsinszky, A.; Philipsen, P. H. T.; Lebègue, S.; Paier, J.; Vydrov, O. A.; Ángyán, J. G. Assessing the Performance of Recent Density Functionals for Bulk Solids. *Phys. Rev. B: Condens. Matter Mater. Phys.* **2009**, *79*, 155107.

(53) Perdew, J. P.; Burke, K.; Ernzerhof, M. Generalized Gradient Approximation Made Simple. *Phys. Rev. Lett.* **1996**, *77*, 3865−3868.

(54) Perdew, J. P.; Ruzsinszky, A.; Csonka, I.; Vydrov, O. A.; Scuseria, G. E.; Constantin, L. A.; Zhou, X.; Burke, K. Restoring the Density-Gradient Expansion for Exchange in Solids and Surfaces. *Phys. Rev. Lett.* **2008**, *100*, 136406.

(55) He, L.; Liu, F.; Hautier, G.; Oliveira, M. J. T.; Marques, M. A. L.; Vila, F. D.; Rehr, J. J.; Rignanese, G.-M.; Zhou, A. Accuracy of Generalized Gradient Approximation Functionals for Density Functional Perturbation Theory Calculations. *Phys. Rev. B: Condens. Matter Mater. Phys.* **2013**, *89*, 064305.

(56) Perdew, J. P.; Levy, M. Physical Content of the Exact Kohn-Sham Orbital Energies: Band Gaps and Derivative Discontinuities. *Phys. Rev. Lett.* **1983**, *51*, 1884−1887.

(57) Dudarev, S. L.; Botton, G. A.; Savrasov, S. Y.; Humphreys, C. J.; Sutton, A. P. Electron-energy-loss spectra and the structural stability of nickel oxide: An LSDA+U study. *Phys. Rev. B: Condens. Matter Mater. Phys.* **1998**, *57*, 1505−1509.

(58) Rohrbach, A.; Hafner, J.; Kresse, G. Ab Initio Study of the (0001) Surfaces of Hematite and Chromia: Influence of Strong Electronic Correlations. *Phys. Rev. B: Condens. Matter Mater. Phys.* **2004**, *70*, 125426.

(59) Brookes, C.; Wells, P. P.; Dimitratos, N.; Jones, W.; Gibson, E. K.; Morgan, D. J.; Cibin, G.; Nicklin, C.; Mora-Fonz, D.; Scanlon, D. O.; Catlow, C. R. A.; Bowker, M. The Nature of the Molybdenum Surface in Iron Molybdate. the Active Phase in Selective Methanol Oxidation. *J. Phys. Chem. C* **2014**, *118*, 26155−26161.

(60) Blöchl, P. E. Projector Augmented-Wave Method. *Phys. Rev. B: Condens. Matter Mater. Phys.* **1994**, *50*, 17953−17979.

(61) Lunt, R. A.; Jackson, A. J.; Walsh, A. Dielectric Response of Fe$_2$O$_3$ Crystals and Thin Films. *Chem. Phys. Lett.* **2013**, *586*, 67−69.

(62) Shull, C. G.; Strauser, W. A.; Wollan, E. O. Neutron Diffraction by Paramagnetic and Antiferromagnetic Substances. *Phys. Rev.* **1951**, *83*, 333−345.

(63) Chen, L.; Shi, C.; Li, X.; Mi, Z.; Wang, D.; Liu, H.; Qiao, L. Strain Effect on Electronic Structure and Work Function in α-Fe$_2$O$_3$ Films. *Materials* **2017**, *10*, 273.

(64) Kiejna, A.; Pabisiak, T. Mixed Termination of Hematite (α-Fe$_2$O$_3$)(0001) Surface. *J. Phys. Chem. C* **2013**, *117*, 24339−24344.

(65) Bergermayer, W.; Schweiger, H.; Wimmer, E. Ab Initio Thermodynamics of Oxide Surfaces: O$_2$ on Fe$_2$O$_3$ (0001). *Phys. Rev. B: Condens. Matter Mater. Phys.* **2004**, *69*, 195409.

(66) Watson, G. W.; Kelsey, E. T.; de Leeuw, N. H.; Harris, D. J.; Parker, S. C. Atomistic Simulation of Dislocations, Surfaces and Interfaces in MgO. *J. Chem. Soc., Faraday Trans.* **1996**, *92*, 433.

(67) Reuter, K.; Scheffler, M. Composition, Structure, and Stability of RuO$_2$ (110) as a Function of Oxygen Pressu. *Phys. Rev. B: Condens. Matter Mater. Phys.* **2001**, *65*, 035406.

(68) Taylor, F. H.; Buckeridge, J.; Catlow, C. R. A. Defects and Oxide Ion Migration in the Solid Oxide Fuel Cell Cathode Material LaFeO3. *Chem. Mater.* **2016**, *28*, 8210−8220.

(69) Morgan, B. J.; Watson, G. W. Intrinsic N-Type Defect Formation in TiO$_2$: A Comparison of Rutile and Anatase from GGA +U Calculations. *J. Phys. Chem. C* **2010**, *114*, 2321−2328.

(70) Swallow, J. E. N.; Williamson, B. A. D.; Whittles, T. J.; Birkett, M.; Featherstone, T. J.; Peng, N.; Abbott, A.; Farnworth, M.; Cheetham, K. J.; Warren, P.; Scanlon, D. O.; Dhanak, V. R.; Veal, T. D. Self-Compensation in Transparent Conducting F-Doped SnO$_2$. *Adv. Funct. Mater.* **2018**, *28*, 1701900.

(71) Chase, M. W., Jr. *NIST-JANAF Thermochemical Tables*, 4th ed. Journal of Physical and Chemical Reference Data Monographs; American Institute of Physics, 1998, Vol. 9, p 1.